## Limits of Spatial Resolution of Phase Encoding Dimensions in MRI of Metals

S. Chandra Shekar<sup>1,4\*</sup>, Daniel T. Hallinan Jr.<sup>1,2,3</sup>, Deanne M. Taylor<sup>4,5</sup> and Eduard Y. Chekmenev <sup>6,7\*</sup>

1. Dept. of Chemical and Biomedical Engineering, Florida A&M University-Florida State University College of Engineering, Tallahassee, FL 32310.

2. Aero-propulsion, Mechatronics and Energy Center, Florida State University, Tallahassee, FL 32310.

3. The National High Magnetic Field Laboratory, Florida State University, Tallahassee, FL 32310.

4. Department of Biomedical and Health Informatics, The Children's Hospital of Philadelphia, Philadelphia, PA 19041.

 $5.\ Department\ of\ Pediatrics,\ Perelman\ School\ of\ Medicine,\ University\ of\ Pennsylvania,\ Philadelphia,\ Pennsylvania,\ 19104.$ 

6. Department of Chemistry + Karmanos Cancer Institute and Integrative Biosciences, Wayne State University, Detroit, MI 48202.

7. Russian Academy of Sciences, Leninskiy Prospekt 14, Moscow, 119991, Russia.

\* Corresponding authors: shekars@email.chop.edu; chekmenev@wayne.edu

A common misperception is that there is no broadening (blurring) along a phase encoded indirect dimension of a multidimensional MRI experiment, despite the celebrated analyses tracing the loss of resolution of image features to truncated data (finite resolution) along that dimension. Here we develop a rule of thumb that, the half width at half maximum (HWHM) of the broadening furnction,  $\delta \approx 0.6\Delta$ , where  $\Delta$  is the resolution or the pixel size along that dimension. We provide experimental evidence corroborating this principle. Parallel is drawn to 2d NMR with *constant time* indirect dimension, to that of phase encoding dimension in 2d MRI.

Magnetic resonance imaging (MRI) is a household name as a powerful, yet noninvasive diagnostic tool in medical field, 1-3 accompanied by additional broad range of applications in many other fields, including the study of materials, 4-7 corrosion of metals, 8 monitoring batteries, fuel cells and supercapacitors. 9-11 On the other hand, MRI of metals has been pioneered only recently. 12-20 It is a revolutionary technology that combines the importance and ubiquitousness of metals with a popular, nondestructive technique such as MRI. In recent years, studies based on breakthrough insights helped overcome challenges inherent to the MRI of metals and demonstrate the applicability of the technique across a broad range. Nevertheless, studies continue to unearth aspects unique to metal MRI (for example, the effective voxel size<sup>19</sup>), which is intimately tied to the propagation of radio frequency (r.f.) electromagnetic (EM) fields inside metals.21-26

In multidimensional MRI, one of the dimensions is directly observed and is quantum mechanically distinct from the indirect dimensions.<sup>4,5,27</sup> In practice, the indirect dimensions can be encoded very differently from the direct dimension by what is known as phase encoding.<sup>4,5</sup> Yet another feature of metal

MRI that we have phenomenologically observed, and that merits reporting, is the broadening in the phase encoded dimension of a 2d MRI experiment.

Like any imaging or spectroscopic technique, MRI images suffer from blurring. Blurring along direct dimension is easy to understand and ascribed to relaxation decay. For the phase encoded dimension, from conventional MRI theory, it is well known that the relaxation decay results only in an overall intensity scaling, without any accompanying blurring. MRI theory also informs that the overall blurring is caused by 'sinc wrapping' associated with data truncation. However, conventionally this is not associated with a characteristic linewidth (like in directly detected dimension), resulting in the tacit assumption that there is no blurring in the phase encoded dimension. Attention is drawn here to a parallel situation in 2d NMR with *constant time* indirect dimension experiments.<sup>27</sup>

However, when attempting to simulate MRI images of metals, we were forced to confront the issue that there is actually blurring characterized by a well defined HWHM, along phase encoded dimension. In a conceptual leap, we recognized that the 1/2 width of the central lobe of 'sinc' function can be used as HWHM for a generic blurring or point spread function (PSF). This led to a surprisingly simple 'rule of thumb' connecting broadening to finite resolution along phase encoded dimension.

In two-dimensional MRI experiments employing phase encoding along the indirect dimension (see Figure S1), there is no relaxation decay along this dimension. Hence, unlike in the directly detected, frequency encoded dimension, the broadening (blurring) does not arise from the relaxation decay. However, the finite (limited) resolution  $\Delta$  (which is also the *pixel* size) along this dimension, naturally gives rise to *sinc* wrapping, as shown in **Supporting Information** (SI) Eqs.(S17) and (S18) based on quantum mechanical density matrix calcu-

1

lations.<sup>4,5,27–30</sup> Here we propose that this blurring be described by a general (for e.g., Gaussian) point spread function (PSF) whose half width at half maximum (HWHM) is given by (see Eqs.(S24),(S25),(S26))

$$\delta \approx 0.6\Delta \tag{1}$$

This was confirmed by analyzing a variety of 2d and 3d MRI experimental images, employing phase encoding along indirect dimensions. We were able to successfully simulate<sup>31</sup> the experimental images by a convolution of effective voxel sizes put forward recently,<sup>19</sup> with a Lorentz-Gauss function<sup>17</sup> characterized by HWHM in the vicinity of nominal HWHM given by the rule of thumb, Eq.(1).

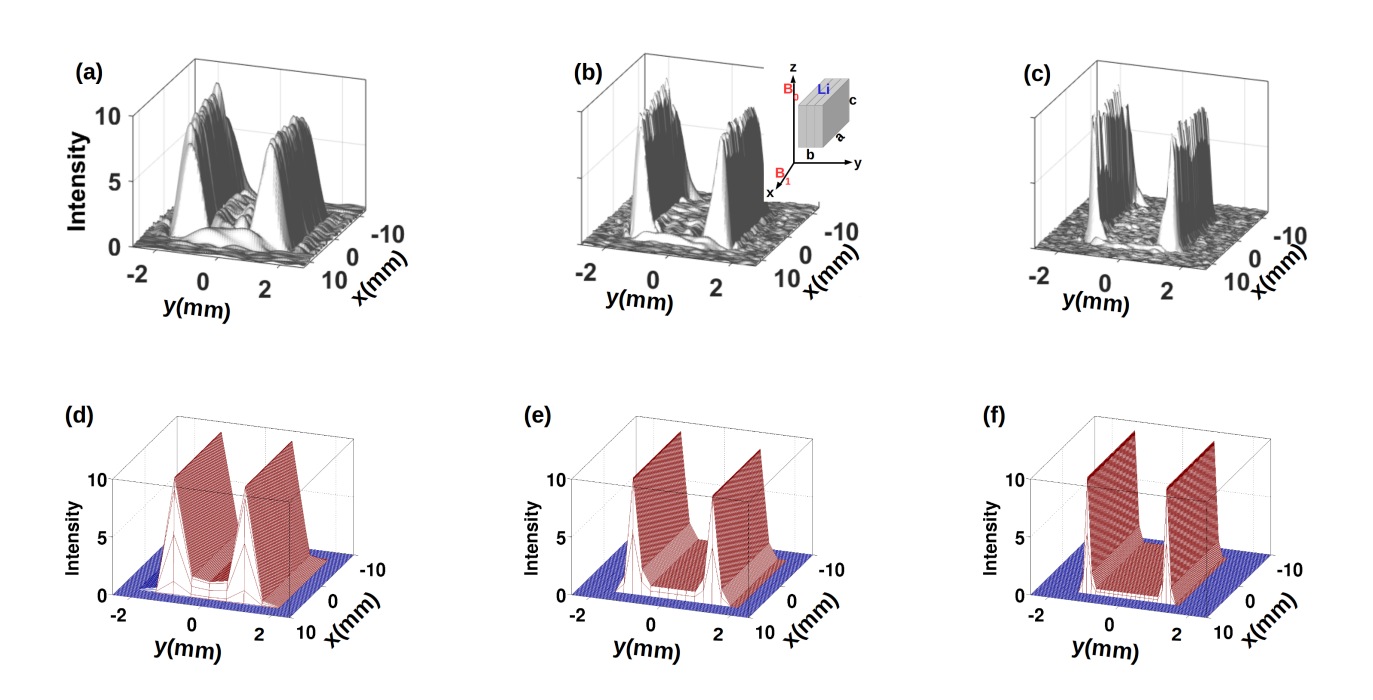


**FIG. 1.**  $^7$ **Li 2d MRI**(xy). 2d MRI(xy) images of an Li metal strip (inset of Panel-(b)), with intensity along vertical axis in arbitrary units. Panels-(a), (b), (c): **experimental** images with increasing resolution along  $y - -\Delta y$ (mm)= 0.5, 0.25, 0.125. Panels-(d), (e), (f): Corresponding **simulations** in with  $\delta y$ (mm)= 0.225, 0.15 and 0.075.

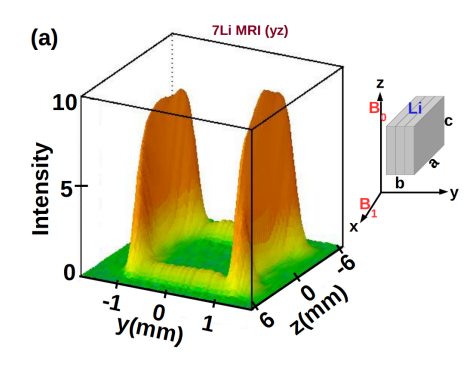
Experimental 2d MRI(xy) images are presented in Figure 1a-c. Here, y is the phase encoded dimension. Panels-(a), (b), (c), display images acquired with progressively increasing resolution by factors of 1, 2, 4, along y dimension, with  $\Delta y$  (mm)= 0.5, 0.25, 0.125 respectively. These in turn, from Eq.(1), give rise respectively to nominal HWHM of  $\delta y$ (mm)  $\approx$  0.3, 0.15 and 0.075. Simulations employing values very close to these, namely,  $\delta y$ (mm)= 0.225, 0.15, 0.075 are shown in panels-(d), (e), (f). These simulations match quite well with the experiment and help reduce the gap between the experimental intensity patterns and those expected from skin depth arguments alone or even the vastly better derived images. <sup>19</sup>

For the experimental 2d MRI(yz) image in Figure 2a, phase encoded dimension is along z, with a resolution of  $\Delta z$ =1 mm. The nominal line broadening from Eq.(1), would be  $\delta z$ = 0.6 mm. We found that  $\delta z$ =0.5 mm mimics the intensity pattern of the experimental image remarkably well, as shown in Figure 2b. Once again, the simulated image is the closest realization to the experimental image. Like for the case of 2d MRI(xy)

images, the match is way better than either the *expected* (from skin depth arguments alone), or even the much better *derived* intensity patterns.<sup>19</sup>

Chemical shift imaging (CSI) is the subject of Figures 3 and 4. CSI combines MRI with NMR, thus correlating spatial distribution with information about chemical environment. A,5,12,31–34 In CSI, one of the axes is NMR chemical shift, whilst the remaining are imaging dimensions. Due to bulk magnetic susceptibility (BMS), the *chemical shift* (CS) of the nuclear spins depends on the orientation of the metal strip face relative to  $\mathbf{B_0}$ . A, 12,13,16,35–38 For the configuration in our case, the BMS effect leads to *two* distinct chemical shifts, one for faces  $\parallel$  to  $\mathbf{B_0}$  and the other for faces  $\perp$  to  $\mathbf{B_0}$ , respectively denoted by  $\Omega_{ac}$  and  $\Omega_{ab}$  (bc faces, being  $\perp$  to  $\mathbf{B_1}$ , do not contribute to MR signal 2,19).

In 3d CSI(yz) (Figure 3), the different regions of 2d MRI(yz) (Figure 2), are now *separated* according to their CS, along the additional CS dimension. In Figures 3 and 4, Panel-(a) displays experimental CSI and Panel-(b) the corresponding simulation. The imaging dimensions are y and z for 3d and y for 2d; CS is



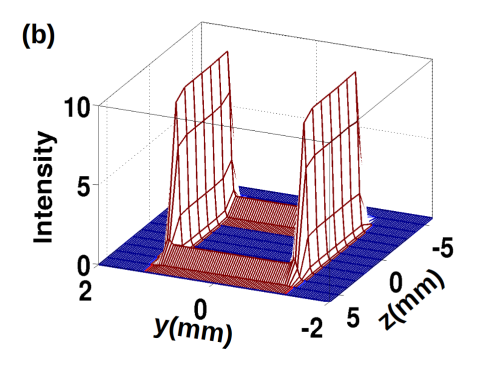


**FIG. 2.** <sup>7</sup>Li **2d MRI**(yz). 2d MRI(yz) images of an Li metal strip (inset of Panel-(a)), with intensity along vertical axis in arbitrary units. *Panel-a*: **Experiment**, <sup>19</sup>  $\Delta z$ = 1 mm. *Panel-b*: **Simulation**, <sup>31</sup>  $\delta z$ = 0.5 mm.

the remaining dimension. The imaging dimensions, were phase encoded.

In 3d CSI(yz),  $\Delta y$ =0.5 and  $\Delta z$ =1 mm, and nominally from Eq.(1),  $\delta y$ =0.3 and  $\delta z$ =0.6 mm. On the other hand, for 2d CSI(y),  $\Delta y$ =0.25 mm and from Eq.(1)  $\delta y$ =0.15 mm. The 3d simulation, to produce a good match with the experiment, required  $\delta y$ =0.3 mm and  $\delta z$ =0.5 mm., Similarly, the 2d simulation produced good match with the corresponding experimental image by using  $\delta y$ =0.2 mm. Thus, once again Eq.(1) aids in arriving at a suitable HWHM value along the phase encoding dimension, to be used in simulations that yield good match with the experiment.

Dielectric MRI images of a non-metallic sample is shown in Figures S2 and S3; panel-(a) displays experiment, with simulations in the corresponding panel-(b). For simulations, for phase encoding dimension, Eq.(1), provided suitable initial value for  $\delta$ , quite close to the final adjusted value to provide good match with experiment.

Thus, the simple rule of thumb in Eq.(1) is important, since one can estimate the extent of blurring (along phase encoded dimension) at a glance using it. What is more, by freeing it from being exclusively associated with the celebrated *sinc* wrap feature, it can serve as a nominal starting value for HWHM of a user specified PSF (for instance Lorentz-Gauss<sup>17,31</sup>) along phase encoded dimension, enabling development of simulations in a facile manner. In addition Eq.(1) is equally applicable to *constant time* indirect dimension of a 2d NMR experiment,<sup>27</sup>

with  $\delta$  and  $\Delta$  now having dimensions of frequency instead of length.

It is interesting to note that in our case, broadening in the indirect phase encoded dimension arose in the context of developing a systematic procedure to simulate new metal MRI intensity patterns unearthed recently.<sup>31</sup> Such efforts may lead the way to develop corrective algorithms (post acquisition, or even real time), that take into account systematic distortions inherent to metal MRI (or, dielectric MRI in the presence or vicinity of metal). Hence, an in-depth understanding of the broadening in the indirect dimension may have wide applicability to those working in the field of metal MRI, and MRI in general, since the underlying physics is the same.

MRI of metals is a fast-emerging field that is rapidly expanding in applications across many fields. The findings presented here may impact (via fresh insights for analysis and interpretation) metal MRI and CSI studies (and have the noninvasive diagnostic potential) for structure of metals and alloys, <sup>39,40</sup> metallurgy (metal fatigue, fracture, strain), <sup>41–44</sup> catalysis, <sup>45–47</sup> metal surface science and surface chemistry, <sup>8,48–55</sup> batteries, fuel cells and supercapacitors, <sup>11,56–58</sup> metallic medical implants and dielectric MRI in the vicinity of metals. <sup>59–71</sup> Given the basic nature of the findings, the approach presented here is likely to

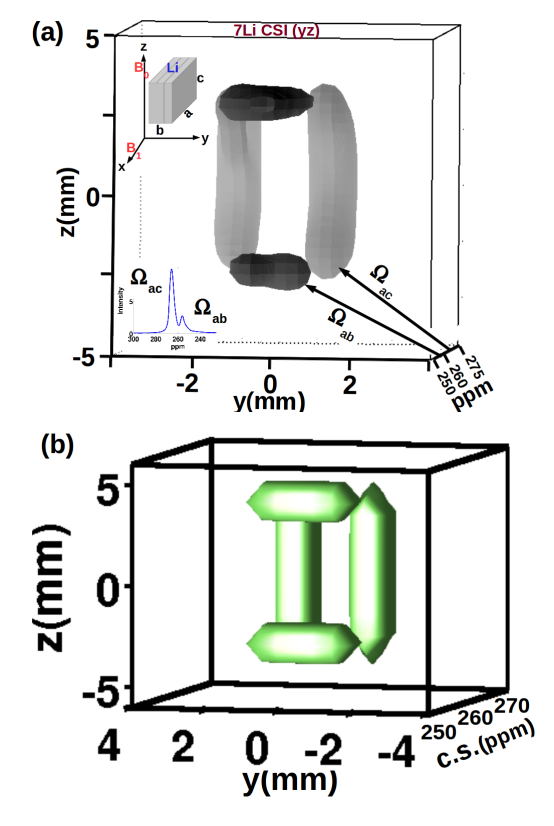


FIG. 3. 3d Chemical Shift Imaging of a lithium metal strip.  $^7\text{Li}$  3d CSI(yz) of a lithium metal strip (inset of Panel-(a)). Panel-(a): Experiment.  $^{19}$  Panel-(b): Simulation.  $^{31}$  The imaging dimensions are y and z, while CS is the remaining dimension. Due to bulk magnetic susceptibility, the MR signal bearing ab and ac faces suffer different CS ( $\Omega_{ab}$ =255 and  $\Omega_{ac}$ =265 ppm respectively), being  $\bot$  and  $\parallel$   $\mathbf{B_0}$  respectively (bc faces, being  $\bot$   $\mathbf{B_1}$  are absent).  $^{19}$   $\Delta y$ =0.5 and  $\Delta z$ =1 mm. For the corresponding simulation,  $\delta y$ =0.3 and  $\delta z$ =0.5 mm.

benefit from advances made in the mainstream (medical) MRI field

## ASSOCIATED CONTENT

### **Supporting Information**

Derivation of the 'Rule of Thumb', Eq.(1), from first principles, simulation of experimental dilectric (non metallic) MRI. The Supporting Information is available free of charge at http://pubs.acs.org.

## **AUTHOR INFORMATION**

**Corresponding Authors** (email):

shekars@email.chop.edu chekmenev@wayne.edu

## **ACKNOWLEDGEMENTS**

SCS thanks: Peter L. Gor'kov and Dr.W.W.Brey (NMR r.f.lab, NHMFL, Tallahassee, FL) for helpful discussions, Prof. Lars Madsen (Dept. of Math., Aahrus University) for help with La-TeX, Ruining Zhang (U.C.S.B., CA) and Devin Bautista-Leaf (Florida State U.) for help with figures and formatting.

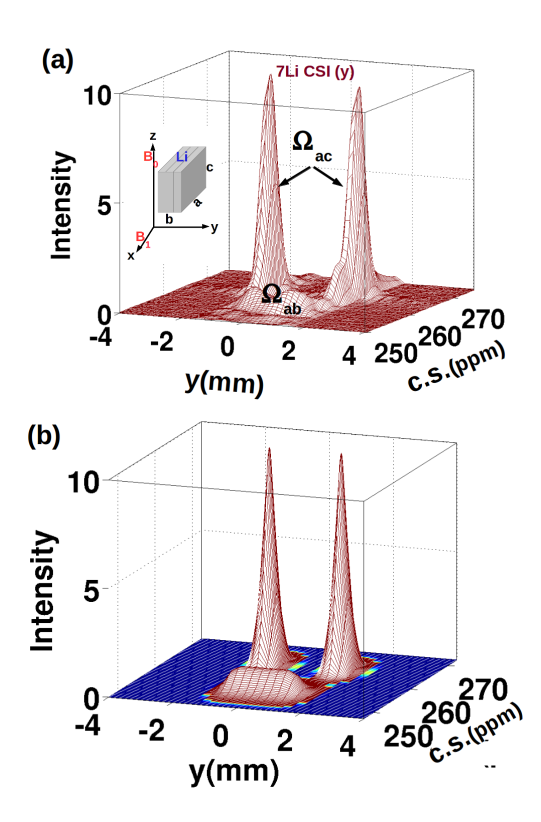


FIG. 4. 2d Chemical Shift Imaging of a lithium metal strip.

<sup>7</sup>Li 2d CSI(y) of a lithium metal strip (inset of Panel-(a)), with vertical axis denoting intensity in arbitrary units. Panel-(a): **Experiment.**<sup>19</sup> Panel-(b): **Simulation.**<sup>31</sup> The imaging dimension is y while the CS is the remaining dimension.  $\Delta y$ =0.25 mm. For simulation,  $\delta y$ =0.2 mm. For further details see Figure 3.

### **REFERENCES**

- C. Westbrook, C. K. Roth, and J. Talbot. MRI in Practice. John Wiley, (2011)
- Thomas E. Yankeelov, David R. Pickens, Ronald R. Price. Quantitative MRI in Cancer. CRC Press, (2011).
- 3. Vincent Perrin. MRI Techniques. John Wiley & Sons, (2013).
- Paul T. Callaghan. Principles of Nuclear Magnetic Resonance Microscopy. Oxford Univ. Press, (2003)
- E. Mark Haacke, Robert E. Brown, Michael R. Thompson and Ramesh Venkatesan. Magnetic Resonance Imaging: Physical Principles and Sequence Design. John Wiley & Sons, Inc., (1999)
- 6. B. Blumich. NMR Imaging of Materials. Oxford University Press, (2003).
- V. S. Bajaj, J. Paulsen, E. Harel and A. Pines. Zooming in on microscopic flow by remotely detected MRI. Science, (2010), 330, 1078-1081.
- 8. A. J. Davenport, M. Forsyth and M. M. Britton. Visualisation of chemical processes during corrosion of zinc using magnetic resonance imaging. *Electrochem. Commun.*, (2010), **12**, 44-47.
- Wang, M., Feindel, K. W., Bergens, S. H. and Wasylishen, R. E. In situ quantification of the in-plane water content in the Nafion membrane of an operating polymer-electrolyte membrane fuel cell using 1H micromagnetic resonance imaging experiments. J. Power Sources, (2010), 195, 7316-7322.
- Z. Zhang and B. J. Balcom, in PEM Fuel Cell Diagnostic Tools. (eds: Wang, H., Yuan, X. and Li, H.) Taylor and Francis, (2011), 229-254.
- Andrew J. Ilott, Nicole M. Trease, Clare P. Grey, and Alexej Jerschow. Multinuclear in situ magnetic resonance imaging of electrochemical double-layer capacitors. *Nature Communications*, (2014), DOI: 10.1038/ncomms5536.
- S. Chandrashekar, Nicole M. Trease, Hee Jung Chang, Lin-Shu Du, Clare P. Grey and Alexej Jerschow. <sup>7</sup>Li MRI of Li batteries reveals location of microstructural lithium. *Nature Materials*, (2012), 11, 311-315.
- Andrew J. Ilott, S. Chandrashekar, Andreas Kloeckner, Hee Jung Chang, Nicole M. Trease, Clare P. Grey, Leslie Greengard, Alexej Jerschow. Visualizing skin effects in conductors with MRI: <sup>7</sup>Li MRI experiments and calculations. *J. Magn. Reson.*, (2014), 245, 143-149.
- Konstantin Romanenko, Maria Forsyth, Luke A. O'Dell. New opportunities for quantitative and time efficient 3D MRI of liquid and solid electrochemical cell components: Sectoral Fast Spin Echo and SPRITE. J. Magn. Reson., (2014), 248, 96-104.
- Melanie M. Britton. Magnetic resonance imaging of electrochemical cells containing bulk metal. Chem. Phys. Chem., (2014), 15, 1731-1736.
- 16. Hee Jung Chang, Andrew J. Ilott, Nicole M. Trease, Mohaddese Mohammadi, Alexej Jerschow, and Clare P. Grey. Correlating microstructural lithium metal growth with electrolyte salt depletion in lithium batteries using <sup>7</sup>Li MRI. J. Am. Chem. Soc., (2015), 137, 15209-15216.
- S. Chandrashekar, Onyekachi Operaji, Guang Yang, and Danliel T. Hallinan Jr. Communication: <sup>7</sup>Li MRI unveils concentration dependent diffusion in polymer electrolyte batteries. J. Electrochem. Soc., (2016) 163 A2988-A2990. [DOI: 10.1149/2.0681614jes]
- Andrew J. Ilott, Mohaddese Mohammadi, Hee Jung Chang, Clare P. Grey and Alexej Jerschow. Real time 3D imaging of microstructure growth in battery cells using indirect MRI. Proc. Natl. Acad. Sci, (2016). 113 (39), 10779â^10784.
- Chandrika S. Chandrashekar, Annadanesh Shellikeri, S. Chandrashekar, Erika Ann Taylor and Deanne Marie Taylor. Visualizing Electromagnetic Fields in metals by MRI. AIP Advances, (2017), 7, 025310. http://dx.doi.org/10.1063/1.4977700
- Andrew J. Ilott, Alexej Jerschow. Super-resolution surface microscopy of conductors using magnetic resonance, Sci. Rep., (2017), 7, 5424.
- 21. Julius Adams Stratton. Electromagnetic Theory. McGraw-Hill, (1941)

- Wolfgang K. H. Panofsky and Melba Phillips. Classical Electricity and Magnetism. Addison-Wesley, (1962)
- 23. Paul Lorrain and Dale R. Corson. **Electromagnetic Fields and Waves.** W. H. Freeman and Company, San Francisco, (1972)
- James D. Jackson. Classical Electrodynamics. John Wiley & Sons, Inc. (1990), 3<sup>rd</sup> edition
- Fawwaz T. Ulaby. Fundamentals of Applied Electromagnetics. Prentice-Hall Inc., (1997), 2001 media edition, Upper Saddle River, New Jersey, 07458, USA.
- 26. David J. Griffiths. Introduction to Electrodynamics. Pearson Education Inc., (1999)  $3^{rd}$  edition, Upper Saddle River, New Jersey, 07458, USA.
- Richard R. Ernst, Geoffrey Bodenhausen and Alexander Wokaun. Principles of Nuclear Magnetic Resonance in One and Two Dimensions. Clarendon Press, Oxford. (1987)
- Paul Adrien Maurice Dirac. The Principles of Quantum Mechanics. Oxford University Press. (1958)
- S. Chandra Shekar, Jonathan M. Backer and Mark E. Girvin. Effectively doubling the magnetic field in spin-½—spin-1, HSQC, HDQC, coupled HSQC, and coupled HDQC in solution NMR. J. Chem. Phys., (2008), 128, 184501. DOI: 10.1063/1.2906116"
- S. Chandra Shekar, Peng Rong, Alexej Jerschow. Irreducible spherical tensor analysis of quadrupolar nuclei. Chem. Phys. Letters, (2008), 464 235. doi:10.1016/j.cplett.2008.08.072
- 31. S. Chandra Shekar, Deanne M. Taylor, Devin Bautista-Leaf, Eduard Y. Chekmenev **Intensity patterns in MRI and CSI of metals.** *Manuscript under preparation.* (2018)
- M. Giesecke, S. V. Dvinskikh and I. Furo. Constant-time chemical-shift selective imaging. J. Magn. Reson., (2013), 226, 19-21.
- Kirk W. Feindel. Spatially resolved chemical reaction monitoring using magnetic resonance imaging. Magn. Reson. Chem., (2015), doi:10.1002/mrc.4179.
- Nils Spengler, Jens Hoefflin, Ali Moazenzadeh, Dario Mager, Neil MacKinnon, Vlad Badilita, Ulrike Wallrabe, Jan G. Korvink. Heteronuclear micro-Helmholtz coil facilitates μm-range spatial and sub-Hz spectral resolution NMR of nL-volume samples on customisable microfluidic chips. PLoS ONE, (2016), 11, doi:10.1371/journal.pone.0146384.
- Rangeet Bhattacharyya, Baris Key, Hailong Chen, Adam S. Best, Anthony F. Hollenkamp, Clare P. Grey. In situ NMR observation of the formation of metallic lithium microstructures in lithium batteries. *Nature Materials*, (2010), 9, 504-510.
- R. E. Hoffman. Measurement of magnetic susceptibility and calculation of shape factor of NMR samples. J. Magn. Reson., (2006), 178, 237-247.
- Lina Zhou, Michal Leskes, Andrew J. Ilott, N. M. Trease, Clare P. Grey. Paramagnetic electrodes and bulk magnetic susceptibility effects in the in situ NMR studies of batteries: application to Li<sub>1.08</sub>Mn<sub>1.92</sub>O<sub>4</sub> spinels. J. Magn. Reson., (2013), 234, 44-57.
- 38. Hee Jung Chang, Nicole M. Trease, Andrew J. Ilott, Dongli Zeng, Lin-Shu Du, Alexej Jerschow, and Clare P. Grey. Investigating Li microstructure formation on Li anodes for lithium batteries by in situ <sup>6</sup>Li/<sup>7</sup>Li NMR and SEM. J. Phys. Chem. C, (2015), 119, 16443-16451.
- 39. Jose A. Rodriguez, D. Wayne Goodman. The nature of the metal-metal bond in bimetallic surfaces. *Science*, (1992), **257**, 897-903.
- 40. C. P. Flynn. Point defect reactions at surfaces and in bulk metals. *Physical Review B*, (2005), **71**, 085422.
- L. Gireaud, S. Grugeon, S. Laruelle, B. Yrieix and J. M. Tarascon. Lithium metal stripping/plating mechanisms studies: A metallurgical approach. *Electrochem. Commun.*, (2006), 8, 1639-1649.
- B.P.P.A. Gouveia, J.M.C. Rodrigues, P.A.F. Martins. Fracture predicting in bulk metal forming. *International Journal of Mechanical Sciences*, (1996), 38, 361-372.
- C.J. Gilbert, R.O. Ritchie, W.L. Johnson Fracture toughness and fatiguecrack propagation in a Zr-Ti-Ni-Cu-Be bulk metallic glass Applied Physics Letters, (1997), 71, 476-478.

- M. Mavrikakis, B. Hammer, J. K. Norskov. Effect of Strain on the Reactivity of Metal Surfaces. *Physical Review Letters*, (1998), 81, 2819-2822.
- L. F. Gladden, M. D. Mantle and A. J. Sederman, Advances in Catalysis, (2006), 50, 1-75. (eds Gates, B. C. and Knozinger, H.) (Elsevier Academic).
- C-J. Zhong, J. Luo, B. Fang, B. N. Wanjala, P. N. Njoki, R. Loukrakpam, Jun Yin. Nanostructured catalysts in fuel cells. *Nanotechnology*, (2010), 21, 062001.
- 47. Fang-Wei Yuan, Hong-Jie Yang, Hsing-Yu Tuan. Seeded silicon nanowire growth catalyzed by commercially available bulk metals: broad selection of metal catalysts, superior field emission performance, and versatile nanowire/metal architectures. *Journal of Materials Chemistry*, (2011), 21, 13793-13800.
- Robert G. Greenler. Infrared Study of Adsorbed Molecules on Metal Surfaces by Reflection Techniques. The Journal of Chemical Physics, (1966), 44, 310-315.
- D W Bassett, M J Parsley Field ion microscope studies of transition metal adatom diffusion on (110), (211) and (321) tungsten surfaces. *Journal of Physics D: Applied Physics*, (1970), 3, 707
- David A. King, Michael G. Wells. Molecular beam investigation of adsorption kinetics on bulk metal targets: Nitrogen on tungsten. Surface Science, (1972), 29, 454-482
- W. Eberhardt, F. Greuter, E. W. Plummer. Bonding of H to Ni, Pd, and Pt Surfaces. Physical Review Letters, (1981), 46, 1085-1088
- 52. J. L. Whitten, H. Yang. Theory of chemisorption and reactions on metal surfaces. Surface Science Reports, (1996), 24, 55-57.
- Gabor A. Somorjai. Modern Surface Science and Surface Technologies: An Introduction. Chemical Reviews, (1996), 96, 1223-1236
- S. Talapatra, S. Kar, S. K. Pal, R. Vajtai, L. Ci, P. Victor, M. M. Shaijumon, S. Kaur, O. Nalamasu and P. M. Ajayan. Direct growth of aligned carbon nanotubes on bulk metals. *Nature Nanotechnology*, (2006), 1, 112-116.
- 55. Zhen Zhang, Junseok Lee, John T. YatesJr., Ralf Bechstein, Estephania Lira, Jonas O. Hansen, Stefan Wendt, Flemming Besenbacher. Unraveling the Diffusion of Bulk Ti Interstitials in Rutile TiO2(110) by Monitoring Their Reaction with O Adatoms. The Journal of Physical Chemistry C, (2010), 114, 3059-3062.
- R. E. Gerald II, R. J. Klingler, G. Sandi, C. S. Johnson, L. G. Scanlon and J. W. Rathke. <sup>7</sup>Li NMR study of intercalated lithium in curved carbon lattices. J. Power Sources, (2000), 89, 237-243.
- 57. M. Klett, M. Giesecke, A. Nyman, F. Hallberg, K. W. Lindstrom, G. Lindbergh, I. Furo. Quantifying mass transport during polarization in a li ion battery by in-situ <sup>7</sup>Li NMR imaging. J. Am. Chem. Soc., (2012), 134, 14654-14657.

- M. M. Britton, P. M. Bayley, P. C. Howlett, A. J. Davenport, M Forsyth. In-situ real time visualization of electrochemistry using magnetic resonance imaging. J. Phys. Chem. Lett., (2013), 3019-3023.
- C. R. Camacho, D. B. Plewes, R. M. Henkelman. Nonsusceptibility artifacts due to metallic objects in MR-imaging. J. Magn. Reson. Imaging, (1995), 5, 75-88.
- L. H. Bennett, P. S. Wang, M. J. Donahue. Artifacts in magnetic resonance imaging from metals. J. App. Phys. (1996), 79, 4712-4714.
- R. V. Olsen, P. L. Munk, M. J. Lee, D. L. Janzen, A. L. MacKay, Q. S. Xiang, B. Masri. Metal artifact reduction sequence: Early clinical applications. *Radiographics*, (2000), 20, 699-712.
- A. M. Viano, S. A. Gronemeyer, M. Haliloglu, F. A. Hoffer. Improved MR imaging for patients with metallic implants. *Magn. Reson. Imag.*, (2000), 18, 287-295.
- 63. M. J. Lee, D. L. Janzen, P. L. Munk, A. MacKay, Q-S Xiang, A. McGowan. Quantitative assessment of an MR technique for reducing metal artifact: application to spin-echo imaging in a phantom. *Skeletal Radiol*, (2001), 30, 398-401.
- F. Shafiei, E. Honda, H. Takahashi, and T. Sasaki. Artifacts from dental casting alloys in magnetic resonance imaging. J. Dent. Res., (2003), 82, 602-606
- 65. H. Graf, G. Steidle, P. Martirosian, U. A. Lauer, F. Schick. **Effects on MRI due to altered RF polarization near conductive implants or instruments.** *Med. Phys.*, (2006), **33**, 124-127.
- M. Moβle, S-I. Han, W.R. Myers, S-K. Lee, N. Kelso, M. Hatridge, A. Pines, J. Clarke. SQUID-detected microtesla MRI in the presence of metal. J. Magn. Reson., (2006), 179, 146-151.
- K. M. Koch, B. A. Hargreaves, K. Butts Pauly, W. Chen, G. E. Gold, K. F. King. Magnetic resonance imaging near metal implants. J. Magn. Reson. Imaging, (2010), 32, 773-778.
- Joseph F. Zikria, Stephen Machnicki, Eugene Rhim, Tandeep Bhatti, Robert E. Graham. MRI of Patients With Cardiac Pacemakers: A review of the medical literature. American Journal of Roentgenology, (2011), 196, 390-401.
- Djaudat Idiyatullin, Curt Corum, Steen Moeller, Hari S. Prasad, Michael Garwood, and Donald R. Nixdorf. Dental MRI: Making the invisible visible. J. Endod., (2011), 37, 745-752.
- Michael Garwood. MRI of fast-relaxing spins. J. Magn. Reson., (2013), 229, 49-54.
- S. Vashaee, F. Goora, M. M. Britton, B. Newling, B. J. Balcom. Mapping B1-induced eddy current effects near metallic structures in MR images: A comparison of simulation and experiment. J. Magn. Reson., (2015), 250, 17-24.

## SUPPORTING INFORMATION

for

# Limits of Spatial Resolution of Phase Encoding Dimensions in MRI of Metals

S. Chandra Shekar<sup>1,4\*</sup>, Daniel T. Hallinan Jr.<sup>1,2,3</sup>, Deanne M. Taylor<sup>4,5</sup> and Eduard Y. Chekmenev <sup>6,7\*</sup>

1. Dept. of Chemical and Biomedical Engineering, Florida A&M University-Florida State University College of Engineering, Tallahassee, FL 32310.

 $2.\ Aero-propulsion, Mechanotronics\ and\ Energy\ Center,\ Florida\ State\ University,\ Tallahassee,\ FL\ 32310.$ 

3. The National High Magnetic Field Laboratory, Florida State University, Tallahassee, FL 32310.

4. Department of Biomedical and Health Informatics, The Children's Hospital of Philadelphia, Philadelphia, PA 19041.

5. Department of Pediatrics, Perelman School of Medicine, University of Pennsylvania, Philadelphia, Pennsylvania, 19104.

6. Department of Chemistry + Karmanos Cancer Institute and Integrative Biosciences, Wayne State University, Detroit, MI 48202.

7. Russian Academy of Sciences, Leninskiy Prospekt 14, Moscow, 119991, Russia.

\* Corresponding authors: shekars@email.chop.edu; chekmenev@wayne.edu

### S1. 2D MRI(YZ) SIGNAL

Consider the 2d MRI(yz) pulse sequence (without slice selection)<sup>1,2</sup> shown in Figure S1.

### pulse sequence for 2d MRI(yz)

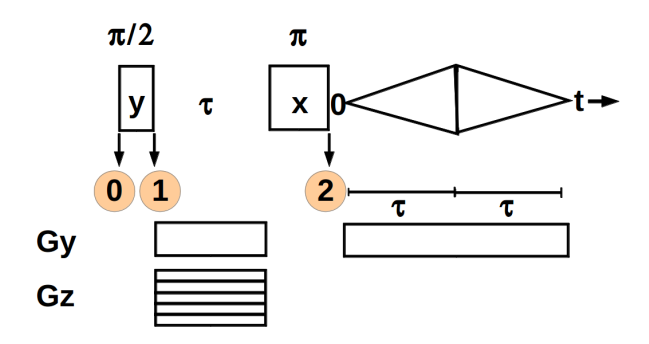


FIG. S1. 2d MRI(yz) pulse sequence.

Frequency encoding along y; phase encoding along z.

Starting from equilibrium magnetization, the evolution of  $\sigma$ , the (quantum mechanical) *density matrix*<sup>1-6</sup> at various stages is outlined below:

At the start,

$$\sigma(0; y, z) = \rho(y, z)\mathbf{I}_{\mathbf{z}} \tag{S1}$$

Above,  $\rho(y,z)$  is the 2d (spin) density that is obtained by summing over the non-imaged dimension x (since there is no slice

selection along x).<sup>1,2</sup>

$$\rho(y,z) = \int dx \, \rho(x,y,z) \tag{S2}$$

Immediately after the  $\frac{\pi}{2}$  r.f. pulse, <sup>1–3</sup>

$$2\sigma(1; y, z) = h.c. + \mathbf{I}_{+} \rho(y, z)$$
 (S3)

where h.c. denotes hermitian conjugate.<sup>4</sup>

Subsequently, the density matrix, just prior to the  $\pi$ -pulse, evolves into

$$2\sigma(\tau; y, z) = h.c. + \mathbf{I}_{+} \rho(y, z) e^{-[R + i\gamma(G_z z + G_y y)]\tau}$$
 (S4)

Above,  $\gamma$  is the *gyromagnetic ratio* of the nucleus giving rise to the MR signal. R is the *characteristic relaxation decay* constant of the MR signal.  $G_{y,z}$  are (magnetic field) gradients applied along y,z respectively.

After the  $\pi$  pulse, (S4) becomes:

$$2\sigma(\tau; y, z) = h.c. + \mathbf{I}_{-} \rho(y, z) e^{-[R + i\gamma(G_z z + G_y y)]\tau}$$
 (S5)

which further evolves into:

$$2\sigma(t; y, z) = h.c. + \mathbf{I}_{-} \rho(y, z) \times e^{-[R + i\gamma(G_z \ z + G_y \ y)]\tau} e^{-[R - i\gamma G_y \ y)]t}$$
(S6)

From quantum mechanics, the **observable** signal is given by 1-6

$$2f(G_z, t; y, z) = 2 tr \{ \mathbf{I}_{+} \boldsymbol{\sigma}(t) \} = \rho(y, z) \times e^{-[R + i\gamma(G_z z + G_y y)]\tau} e^{-[R - i\gamma G_y y)]t}$$
 (S7)

For phase encoded dimension, the gradient is increased by equal increments along z direction (Figure S1) according to:

$$-G_{z0} \le G_z \le G_{z0} \tag{S8}$$

$$0 \le t \le t_{\text{max}} \tag{S9}$$

With the definitions

$$k_{y0} = \gamma G_y \tau; \quad k_y = \gamma G_y t; \Longrightarrow 0 \le k_y \le k_y^{\text{max}}$$
 (S10)

and

$$k_{z0} = \gamma G_{z0} \ \tau \Longrightarrow -k_{z0} \le k_z \le k_{z0} \tag{S11}$$

Eq.(S7) can be rewritten as an explicit function of the two *phase* space variables  $k_z$ ,  $k_y$ , with contribution from 2d spin density at spatial location (y, z):

$$2f(k_z, k_y; y, z) = \rho(y, z) \times e^{-[R\tau + i(k_z z + k_{y0} y)]} e^{-(R_e - iy)k_y}$$
(S12)

 $R_e$ , the *effective* relaxation rate constant given by

$$R_e = R/(\gamma G_y) \tag{S13}$$

The signal from the *entire* sample is obtained by integrating (S12) over y and z.

$$2f(k_z, k_y) = \int dz \int dy \, \rho(y, z) \times \\ e^{-[R\tau + i(k_z \, z + k_{y0} \, y)]} \, e^{-(R_e - iy)k_y}$$
 (S14)

The spin density profile is extracted by 2d Fourier transform (F.T.) of (S14)

$$F(z,y) = \int_{-k_{z0}}^{k_{z0}} dk_z \ e^{-ik_z z} \int_0^{k_y^{\text{max}}} dk_y \ e^{-ik_y y} f(k_z, k_y)$$
(S15)

resulting in:

$$2F(z,y) = e^{-R\tau} \int dz' \int dy' \, \rho(y',z') \, e^{-ik_{y0} \, y'}$$

$$\times \int_{-k_{z0}}^{k_{z0}} dk_{z} \, e^{-ik_{z}(z+z')} \int_{0}^{k_{y0}^{\text{max}}} dk_{y} \, e^{-[R_{e}+i(y-y')]k_{y}}$$
(S16)

finally yielding,

$$F(z,y) = k_{z0}e^{-R\tau} \int dz' \operatorname{sinc} \left[ k_{z0}(z+z') \right]$$

$$\times \int dy' \, \rho(y',z') \, e^{-ik_{y0} \, y'}$$

$$\times \left\{ 1 - e^{-[R_e + i(y-y')]k_y^{\max}} \right\} \mathcal{L} \left( R_e, \, y - y' \right)$$
(S17)

where the function

$$\operatorname{sinc}(\theta) = \sin \theta / \theta \tag{S18}$$

In (S17), the (*complex*) Lorentzian is given by:

$$\mathcal{L}(R_e, y) = \frac{1}{R_e + iy} = \mathcal{A}(R_e, y) + i\mathcal{D}(R_e, y)$$

$$= e^{-i\phi} \mathcal{M}(R_e, y)$$
(S19)

with

$$\tan \phi = y/R_e \tag{S20}$$

The *real* (absorptive), *imaginary* (dispersive) and *magnitude* functions are respectively given by:

$$A = \frac{R_e}{R_e^2 + y^2}; \quad \mathcal{D} = -\frac{y}{R_e}A; \quad \mathcal{M} = \frac{1}{\sqrt{R_e^2 + y^2}}$$
 (S21)

Note that the  $\frac{1}{2}$ -max (HWHM) for  $\mathcal{A}$  occurs at  $y=\pm R_e$  while for  $\mathcal{M}$ , it is at  $y=\pm\sqrt{3}R_e$ . Thus,

$$\delta y_{1/2} \equiv \delta y = R_e \tag{S22}$$

Further,

$$\int_{-\infty}^{\infty} dy \, \mathcal{L}(R_e, y) = \pi \tag{S23}$$

It is less straightforward to assess the broadening in the phase encoding dimension along z. In principle, since there is no relaxation during phase encoding dimension, there is no blurring (broadening) for this dimension. But it is well known<sup>1,2</sup> that because of finite extent of the k-space along this dimension, the resulting image is a convolution of the spin density  $\rho(y,z)$  with the sinc function (see (S17)), with the resultant blurring. From (S18), HWHM for the *central lobe* of  $\sin(\theta)$  occurs at

$$\theta_{1/2} \approx 108.6\pi/180 \text{ radians.}$$
 (S24)

(Note that sinc(0)=1;  $sinc(\pm \pi)=0$ .) Correspondingly (see (S17)),

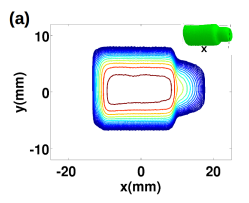
$$\delta z_{1/2} \equiv \delta z = \frac{\theta_{1/2}}{k_{z0}} \approx \frac{108.6}{180} \Delta z \approx 0.6 \Delta z \tag{S25}$$

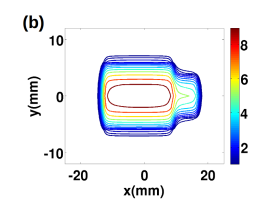
leading to Eq.(1), since, 1,2

$$\Delta z = \pi / k_{z0}; -k_{z0} < k_z < k_{z0}$$
 (S26)

where  $\Delta z$  is the resolution or the pixel size along z.

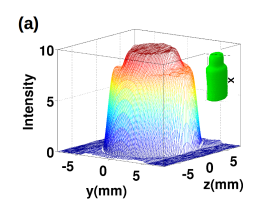
### **S2. DIELECTRIC MRI**





### FIG. S2. $^{7}$ Li 2d MRI(xy) of LiCl solution

LiCl (1M) solution in 2 ml D2O + 50 mM of CuSO4, in a bottle (shown as inset in panel-(a)). The bottle axis  $\parallel x \parallel \mathbf{B_1}$  (see insets in figures in main part, for e.g. Figure 4). Panel-(a): **Experimental**, with pixel size for phase encoding dimension,  $\Delta y = 2$  mm, yielding from Eq.(1), nominal HWHM  $\delta y = 1.2$  mm. Panel-(b): **Simulation**, with  $\delta y = 1.5$  mm., with an admixture of equal amounts of Lorentzian and Gaussian constituting the broadening function.<sup>7,8</sup>



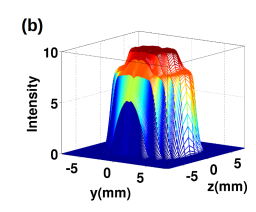


#### FIG. S3. $^{7}$ Li 2d MRI(yz) of LiCl solution,

with intensity along vertical axis in arbitrary units. Sample and its configuration are same as in Figure S2. Panel-(a): **Experimental**, with pixel size for phase encoding dimension,  $\Delta z=1$  mm, yielding from Eq.(1), nominal HWHM  $\delta z=0.6$  mm. Panel-(b): **Simulation**,  $\delta z=0.5$  mm., with a Gaussian broadening function.<sup>7,8</sup>

### REFERENCES

 Paul T. Callaghan. Principles of Nuclear Magnetic Resonance Microscopy. Oxford Univ. Press, (2003)

- E. Mark Haacke, Robert E. Brown, Michael R. Thompson and Ramesh Venkatesan. Magnetic Resonance Imaging: Physical Principles and Sequence Design. John Wiley & Sons, Inc., (1999)
- Richard R. Ernst, Geoffrey Bodenhausen and Alexander Wokaun. Principles of Nuclear Magnetic Resonance in One and Two Dimensions. Clarendon Press, Oxford. (1987)
- 4. Paul Adrien Maurice Dirac. The Principles of Quantum Mechanics. Oxford University Press. (1958)
- S. Chandra Shekar, Jonathan M. Backer and Mark E. Girvin. Effectively doubling the magnetic field in spin-1/2—spin-1, HSQC, HDQC, coupled HSQC, and coupled HDQC in solution NMR. J. Chem. Phys., (2008), 128, 184501. DOI: 10.1063/1.2906116"
- S. Chandra Shekar, Peng Rong, Alexej Jerschow. Irreducible spherical tensor analysis of quadrupolar nuclei. Chem. Phys. Letters, (2008), 464 235. doi:10.1016/j.cplett.2008.08.072
- S. Chandrashekar, Onyekachi Operaji, Guang Yang, and Danliel T. Hallinan Jr. Communication: <sup>7</sup>Li MRI unveils concentration dependent diffusion in polymer electrolyte batteries. J. Electrochem. Soc., (2016) 163 A2988-A2990. [DOI: 10.1149/2.0681614jes]
- S. Chandra Shekar, Deanne M. Taylor, Devin Bautista-Leaf, Eduard Y. Chekmenev Intensity patterns in MRI and CSI of metals. Manuscript under preparation. (2018)